Edinburgh Research Explorer

The effect of permeability on the flow past permeable disks at low Reynolds numbers

OPEN ACCESS

The effect of permeability on the flow past permeable disks at low Reynolds numbers

Cathal Cummins, Ignazio Maria Viola, Enrico Mastropaolo, and Naomi Nakayama

Articles you may be interested in

Instability of a binary liquid film flowing down a slippery heated plate
Physics of Fluids **29**, 092105 (2017); 10.1063/1.4989558

Interaction of vortex ring with a stratified finite thickness interface
Physics of Fluids **29**, 093602 (2017); 10.1063/1.4994264

 Novel criteria for the development of monotonic and oscillatory instabilities in a two-layer film
Physics of Fluids **29**, 092104 (2017); 10.1063/1.5001729

Dispersion-driven instability of mixed convective flow in porous media
Physics of Fluids **29**, 094102 (2017); 10.1063/1.4990386

The rising motion of spheres in structured fluids with yield stress
Physics of Fluids **29**, 093101 (2017); 10.1063/1.4998740

The propulsion of two flapping foils with tandem configuration and vortex interactions
Physics of Fluids **29**, 097102 (2017); 10.1063/1.5001501

The effect of permeability on the flow past permeable disks at low Reynolds numbers

Cathal Cummins,[1,2,3,a)] Ignazio Maria Viola,[1,b)] Enrico Mastropaolo,[4] and Naomi Nakayama[2,3,5]

[1]*Institute for Energy Systems, School of Engineering, University of Edinburgh, EH9 3DW Edinburgh, United Kingdom*
[2]*Institute of Molecular Plant Sciences, School of Biological Sciences, University of Edinburgh, EH9 3BF Edinburgh, United Kingdom*
[3]*SynthSys Centre for Systems and Synthetic Biology, School of Biological Sciences, University of Edinburgh, EH9 3BF Edinburgh, United Kingdom*
[4]*Institute for Integrated Micro and Nano Systems, Scottish Microelectronics Centre, School of Engineering, University of Edinburgh, EH9 3FF Edinburgh, United Kingdom*
[5]*Centre for Science at Extreme Conditions, School of Biological Sciences, University of Edinburgh, EH9 3BF Edinburgh, United Kingdom*

The viscous flow over a thick permeable circular disk in the Reynolds number (Re) range of 10 to 130 and in the Darcy number (Da) range of 10^{-9} to 1 is examined. Direct numerical simulations are performed on a 2D grid with axisymmetric boundary conditions. Three flow regimes are observed: I, II, and III. In regime I (effectively impervious; $Da < 10^{-6}$), the wake is characterized by the presence of a toroidal vortex whose length is approximately equal to that of an impervious disk. In regime II (transition; $10^{-6} < Da < 10^{-3}$), the increase in Da causes the vortex to shorten and move downstream and eventually vanishes at a critical Darcy number Da_c. Regime III ($Da > 10^{-3}$) is the highly permeable regime, in which there is no recirculation. In I, good agreement with existing experimental data for impervious disks is found. In III, an analytical expression for the drag force on the disk is derived, showing good agreement with the numerical results. A global upper limit of $Da_c = Da_{max}$ above which the disk is unable to maintain a recirculating wake for any Re is identified. Finally, in regime II, it is demonstrated that increasing the permeability can lead to large variations in the length of the recirculating wake but with minimal effect on the drag coefficient even when $Da > Da_{max}$. This has important implications in our understanding of the locomotive strategies adopted by organisms that use porous bodies for movement. *Published by AIP Publishing.* [http://dx.doi.org/10.1063/1.5001342]

I. INTRODUCTION

The fluid flow past and through a permeable body is an important problem in many physical applications such as binary alloy solidification,[1] tissue engineering scaffolds in micro-bioreactors,[2] sedimentation in liquid-solid reactors,[3,4] and in the wind dispersal of small plants.[5] For very low permeabilities, permeable bodies interact with the surrounding fluid as though they were impervious to it; hence, many of the results for impervious bodies hold for highly impermeable bodies. As a body's permeability is increased, some interesting features emerge, which distinguish the flow around a permeable body from its impervious counterpart. Many studies have shown that the flow fields around permeable bodies undergo qualitative changes in their structure as the permeability is increased, such as transition from recirculation to shear flow.[4,6–8] Over a large range of permeabilities, the drag force acting on a permeable body differs little from that of an equivalent impervious body.[4] Some insects make use of this

by evolving weight-saving porous wings rather than impervious wings. For example, the millimeter-sized insect wings of *Thrips* (Thysanoptera) are composed of filaments, which are 80 μm in length, 1 μm in diameter, and spaced 20 μm apart;[9] leading to an overall wing porosity of 0.95. These wings supply 90% of the force produced by an impervious wing but weigh about 10% of such a wing.[10] The drag force experienced by permeable bodies such as permeable spheres[3] and permeable cylinders[4,11] can also exceed that of an equivalent impervious body.

The flow around various permeable bodies has been examined in the past: including a 2D permeable square[6] and circular[4,7] cylinder and a permeable sphere.[3,8,12] However, the case of low-Reynolds number (Re) flow past a permeable disk has yet to be considered. The only experiments[13] of the flow past permeable circular disks were conducted using Particle Image Velocimetry (PIV) at high Re. This is surprising, since the literature on the fluid flow past impervious disks is extensive, and their motion is incredibly rich.[14–18] In this paper, we aim to close this gap by examining the effect of finite permeability on the low-Re fluid flow past permeable disks.

a)Electronic mail: Cathal.Cummins@ed.ac.uk
b)Electronic mail: I.M.Viola@ed.ac.uk

An impervious circular disk falling in a viscous fluid at low Reynolds numbers (based on the disk's diameter) experiences one of five possible motions:[14]

1. For $Re \ll 1$: the disk falls steadily maintaining its *initial orientation*.
2. For $1 \lessgtr Re < 100$: the disk falls steadily along its axis, maintains a *horizontal orientation*, and experiences a drag force identical to that of a fixed disk.
3. For $Re > 100$: the motion is generally unsteady and depends on the dimensionless moment of inertia (I^*), which is defined as the ratio of disk's moment of inertia about an axis in the plane of the disk and through its center to that of a rigid sphere of fluid of the same diameter. For small I^*, the disk shows *small regular pitching oscillations* about this axis, without any translational motion.
4. For $Re > 100$ and intermediate I^*: the disk shows a *glide-tumble* motion. The amplitude of the pitching motion defined above is no longer small and becomes chaotic, leading to appreciable translational motion of the disk's center of mass in changing directions.[16]
5. For $Re > 100$ and large I^*: the motion is one of continuous *tumbling* while drifting in one direction.

Once free fall motion becomes unsteady, the mean drag force acting on the disk can differ significantly from that on a fixed disk with steady relative velocity.[15] Fabre, Auguste, and Magnaudet[19] considered the generic problem of wake instabilities past fixed axisymmetric bodies, and they focus on the extreme cases of a sphere and a flat disk. Their numerical results reveal that the wakes of spheres and disks evolve differently as Re is increased and that new vortex shedding modes are found to exist behind a disk, not present for spheres.

Shenoy and Kleinstreuer[18] consider the flow over a thick circular impervious disk of aspect ratio $\chi = 10$ (diameter/thickness) in the Re range of 10–300, using Computational Fluid Dynamics (CFD). They identified five flow regimes depending on the value of Re; the three regimes corresponding to the lowest Re are as follows:

1. $Re < 135$: steady axisymmetric flow with the presence of a toroidal vortex behind the disk;
2. $135 \le Re < 155$: regular bifurcation with loss of azimuthal symmetry but with planar symmetry and a double-threaded wake;
3. $155 \le Re < 172$: three-dimensional flow with periodic shedding of double-sided hairpin-shaped vortex structures and periodic motion of the separation region.

Auguste, Fabre, and Magnaudet[20] study the dynamics of the wake of an impervious circular disk of aspect ratio $\chi = 3$ embedded in a uniform flow, focussing in particular on the range $150 < Re < 218$. As Re is increased, the flow experiences multiple bifurcations, ultimately resulting in a chaotic state.

The case of a permeable bluff body has generally received less attention. The first studies considered the creeping flow ($Re \ll 1$) past a permeable sphere,[12] where the resistance experienced by permeable spheres in creeping flow was always less than that experienced by the equivalent impervious sphere. Feng and Michaelides[21] obtained general expressions for the drag force acting on a permeable sphere at a small but finite Re and observed that this force is always less than the corresponding values of the equivalent impervious sphere. These observations are confirmed in experiments[3] that examined the settling velocities of permeable spheres falling in creeping flow conditions and at small but finite Re. As Re increases ($7 < Re < 120$), however, a permeable sphere actually experienced a higher drag than an equivalent impermeable sphere.[3]

In the experimental studies of high-Re flow past perforated plates,[22] a reversed flow bubble is observed behind the plate, which detaches and moves downstream. There are two distinct regimes of the flow: one appropriate to low values of porosity where the vortex street dominates the wake; the strength of this vortex street gradually decreases as the vorticity in the shear layers decreases with the introduction of bleed air, and the reversed flow region and vortex formation region move downstream. In the other flow regime, corresponding to high porosity, the vortex street is not present at all, and the transition between these two regimes is abrupt.

Noymer, Glicksman, and Devendran[4] considered the case of a permeable circular cylinder at low-to-moderate Re ($10 < Re < 1000$) using a numerical model based on an application of Darcy's law to the region occupied by the cylinder. Consistent with previous studies,[3] the drag force acting on the permeable cylinder can be higher than that of an impermeable cylinder, and these findings were substantiated by wind tunnel measurements on permeable cylinders.[4] There is an emerging literature on the study of the flow past arrays, or patches, of obstacles.[11] Interestingly, the drag coefficient measured for sparse arrays is found to increase with decreasing permeability, reaching a maximum for some finite permeability. This maximum is higher than that found for an equivalent impervious obstacle, in agreement with experiments on permeable spheres[3] and permeable cylinders.[4]

Jue[23] considered the vortex shedding behind a permeable square cylinder using a numerical model based on the Darcy-Brinkman equations for $Re = \mathcal{O}(10^2)$. The flow fields and characteristic values of vortex shedding for Darcy numbers (Da) approaching zero ($Da \le 10^{-6}$) are almost entirely unchanged from that of an impervious square cylinder. A larger Da was found to postpone the occurrence of flow fluctuations. Later, a similar numerical model was used to demonstrate that an increase in Da delays the critical Re at which vortex shedding phenomena occur for permeable square cylinders.[24]

More recently, the steady flow around and through a permeable circular cylinder was studied numerically[7] using the Darcy-Brinkman-Forchheimer equations. The recirculating wake existing downstream of the cylinder is found to either penetrate into or be completely detached from the cylinder; the problem is explored in the Re-Da parameter space. Also presented in the study is the variation of the critical Reynolds number for the onset of a recirculating wake as a function of Da.

To date, the flow past a permeable circular disk at moderate Re has yet to be examined. One particularly interesting feature of all permeable bodies is that at some critical Darcy number, the wake disappears. However, this absolute upper limit on permeability has never been computed for a

permeable body. Furthermore, in all previous studies of permeable bodies, the recirculating wake has always been examined independently from the drag forces experienced by the body. By examining the wake structure and the drag forces together, any regions of the parameter space where these two quantities are decoupled in their dependence on the permeability can be identified. This is an important concept in biology, where the biological function of a permeable body changes as the body's permeability changes.[25] In some organisms, for example, the function of the recirculating wake may be for food capture;[26] other organisms, such as small flying insects, have evolved highly porous wings, which weigh much less than an impervious wing but with little loss in aerodynamic function.[10,27]

The objective of the present study is to characterize the steady flow past a permeable circular disk. We will examine the low-*Re* flow past a permeable disk for a range of permeabilities (characterized by the disk's Darcy number). Three regimes are identified: (I) an effectively impervious regime, (II) a transition regime, and (III) a highly permeable regime. In regime I, the flow quantities approach that of an impervious disk, showing good agreement with existing experimental data; in regime III, the flow is shown to approach a high-permeability limit, within which an asymptotic formulation of the resistance experienced by the disk is derived. The solution in regime II does not yield to an asymptotic analysis and must be explored by solving the original equations numerically, and we show that our results are consistent with previous studies on permeable bodies.[3,4,11,22]

The paper is structured as follows: in Sec. II, the governing equations are written down and non-dimensionalized (Sec. II A), and the numerical procedure and a summary of the uncertainty analysis are presented (Sec. II B). We provide the full details of our uncertainty analysis in Appendix A, including a verification (Appendix A 1) and validation (Appendix A 2) study. The results are presented in Sec. III and discussed in Sec. IV. The paper concludes with a further discussion in Sec. V of the results obtained with reference to existing studies on the flow past permeable bodies.

II. MATHEMATICAL MODEL

A. The governing equations

Consider a permeable circular disk with diameter D', thickness T', isotropic porosity ϵ, and permeability κ' moving along its axis in a viscous fluid with a characteristic velocity of magnitude U', where the primes indicate a quantity with a physical dimension. For an incompressible Newtonian fluid with density ρ' and dynamic viscosity μ', the flow satisfies the steady-state Navier-Stokes equations,

$$\rho'(\mathbf{u}' \cdot \nabla')\mathbf{u}' = -\nabla'p' + \mu'\nabla'^2\mathbf{u}', \qquad (1)$$

in the fluid domain, where the fluid's velocity $\mathbf{u}'(\mathbf{x}')$ is given by $\mathbf{u}' = u_r'\hat{r} + u_z'\hat{z}$, where $p'(\mathbf{x}')$ is the pressure, $\hat{r}$ and $\hat{z}$ are the unit vectors as shown in Fig. 1(a), and u_r' and u_z' are the velocities in the $\hat{r}$- and $\hat{z}$-direction, respectively. The losses in momentum due to the porous medium are incorporated using the Brinkman equations,

$$\rho'\left(\frac{1}{\epsilon^2}\mathbf{u}' \cdot \nabla'\right)\mathbf{u}' = -\nabla'p' + \frac{\mu'}{\epsilon}\nabla'^2\mathbf{u}' - \frac{\mu'}{\kappa'}\mathbf{u}', \qquad (2)$$

and the continuity equation $\nabla' \cdot \mathbf{u}' = 0$ in the porous region. At the interface between the porous region and the fluid domain, continuity of $\mathbf{u}'$ and p' is imposed.

Let us introduce the following non-dimensional variables:

$$\mathbf{u} = \mathbf{u}'/U', \quad p = p'/(\rho'U'^2), \quad \mathbf{x} = \mathbf{x}'/D', \qquad (3)$$

then $\mathbf{u}$ satisfies

$$(\mathbf{u} \cdot \nabla)\mathbf{u} = -\nabla p + \frac{1}{Re}\nabla^2\mathbf{u}, \qquad (4)$$

in the fluid domain, and

$$\left(\frac{1}{\epsilon^2}\mathbf{u} \cdot \nabla\right)\mathbf{u} = -\nabla p + \frac{1}{\epsilon Re}\nabla^2\mathbf{u} - \frac{1}{Da}\frac{1}{Re}\mathbf{u}, \qquad (5)$$

in the porous region, where

$$Re = \frac{U'\rho'D'}{\mu'}, \quad Da = \frac{\kappa'}{D'^2} \qquad (6)$$

are the Reynolds number and Darcy number, respectively. The nondimensional continuity equation,

$$\nabla \cdot \mathbf{u} = 0, \qquad (7)$$

is satisfied throughout the domain. There are four model parameters: Re, Da, ϵ, and the aspect ratio $\chi = D'/T'$. In this study, ϵ is fixed to be 0.95 and χ is fixed at 10.

B. The numerical model

1. Computational domain and grid

The numerical solution to the steady incompressible Navier–Stokes and Brinkman equations, Eqs. (4),(5), and (7), along with their boundary conditions, was computed using the finite-element-based commercial code COMSOL Multiphysics. The half section of the permeable circular disk of diameter D and aspect ratio $\chi = 10$ was modeled by a rectangular box ($0.5D \times 0.1D$) in a 2D-axisymmetric computational domain, Fig. 1(a). The reference system of coordinates (r, z), whose origin is located in the center of the disk, with the z-axis points in the direction of the freestream velocity, and the r-axis lies along the width of the disk. The domain extends $6D$ radially, $15D$ downstream, and $2.5D$ upstream of the disk [see Fig. 1(b)]. Uniform velocity is prescribed at the upstream face of the domain, and slip on the face at $r = 6D$. An axisymmetric symmetry condition was used at $r = 0$ and a constant pressure was imposed at the downstream face. Figure 1(b) shows the H-type grid with 384 and 2016 cells in the radial and streamwise directions, respectively, and the mesh grading near the disk's surface [inset, Fig. 1(b)].

2. Uncertainty and error analysis

Here, the findings of the uncertainty and error analysis are summarized, while full details are provided in Appendix A. To facilitate this study, the uncertainty and error of two quantities are considered: the wake length L and the drag coefficient C_D, at the minimum and maximum Reynolds numbers considered
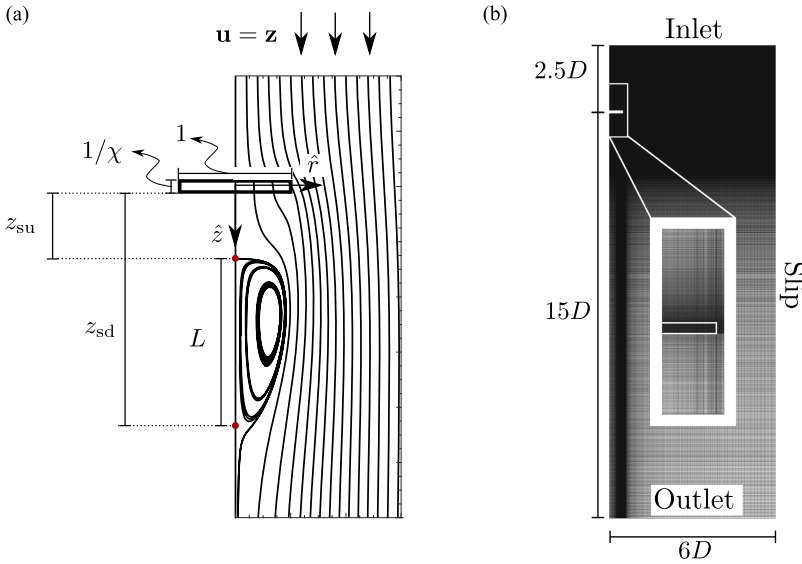
(a)

(b)

FIG. 1. (a) The geometry of the circular disk (section), the wake, and flow streamlines. (b) Overview of the computational grid and detailed view near the disk's surface (inset).

in this study: $Re = 10$ and $Re = 130$. For these two Re, the differences between C_D computed with the reference grid and by halving the number of grid points both streamwise and radially are 0.47% and 0.15% for $Re = 10$ and $Re = 130$, respectively. The differences between L computed with these two grids are 0.14% and 0.02% for $Re = 10$ and $Re = 130$, respectively. These small differences indicate little dependence of the solution on the grid.

The numerical uncertainty is computed taking into account the grid resolution and the iterative error, while the error due to the numerical model considers the effects due to the choice of finite domain. The simulations were run in double precision and for a number of iterations sufficient to have an iterative convergence error that is several orders of magnitude smaller than all other numerical errors (see Appendix A for more details).

The numerical uncertainty U_{num} at a 95% confidence level in both quantities is always less than 1% on the grid used in our study. The uncertainty in C_D is 0.56% for $Re = 10$ and for $Re = 130$ it is 0.20%. The uncertainty U_{num} in the wake length L is 0.13% and 0.22% for $Re = 10$ and $Re = 130$, respectively. We compare our results to experimental data[15] in Appendix A 2 for the case of an impervious disk. We demonstrate that our results are validated for $Re = 130$ and that at low Re, the choice in finite domain size accounts for the small differences between our computed values and the experimental measurements.

III. THE RESULTS

In the Reynolds number range of 10–130, the flow is separated from the leading edge and forms a toroidal vortex behind the disk when Da approaches zero, but this vortex disappears as Da is increased past a critical Darcy number Da_c, which depends on Re. The vorticity increases with Re, as does the length of the recirculating wake (see Figs. 2 and 3). Going from (a) to (d) in Figs. 2 and 3, less vorticity is generated as Da increases from low to high permeability, until a point where there is no recirculation at all.

In order to examine the evolution of the recirculating wake, the position of the stagnation points (z_s) in the flow must be determined. Once the upstream z_{su} and the downstream stagnation points z_{sd} are found, the wake length is given by $L = z_{sd} - z_{su}$. To determine the values of the stagnation points, the axial velocity in the streamwise direction (u_z) is computed; the vortex is present wherever $u_z < 0$.

Qualitatively, there are three cases:

1. For $Da < Da_c$, there are two stagnation points;
2. for $Da > Da_c$, there are no stagnation points, and hence, there is no recirculating vortex;
3. for $Da = Da_c$, the recirculating wake has zero length, and the distance downstream of the disk's rear face at which the two stagnation points annihilate one another is denoted by $d = z_s - 1/(2\chi)$.

The position of the stagnation points in the disk's wake is plotted as a function of Da in Fig. 4(a), for three values of the Reynolds number: $Re = 10$, 30, and 130. Three regimes are identified as follows:

1. An effectively impervious regime, $0 < Da < 10^{-6}$, where the upstream stagnation point (z_{su}) is on the disk's rear face and the downstream stagnation point (z_{sd}) is within 1% of that of a corresponding impervious disk.
2. A transition regime, $10^{-6} < Da < 10^{-3}$, where z_{su} moves downstream towards z_{sd} as Da is increased and z_{sd} generally moves upstream as Da is increased.
3. A highly permeable regime, $Da > 10^{-3}$, where no stagnation points occur.

As Da is increased within the transition regime, the downstream stagnation point generally moves towards the upstream stagnation point; however, it does not follow a monotonic path as Da is increased, and it depends on the value of Re. Consider the $Re = 130$ curve in Fig. 4(a): increasing Da in the transition regime, z_{sd} initially moves downstream [upwards in Fig. 4(a)] and then rapidly moves upstream [downwards in Fig. 4(a)] to meet the other stagnation point in a bifurcation at $Da = Da_c$. At the other three Reynolds numbers, the trend is monotonic: both stagnation points in each case move towards each other
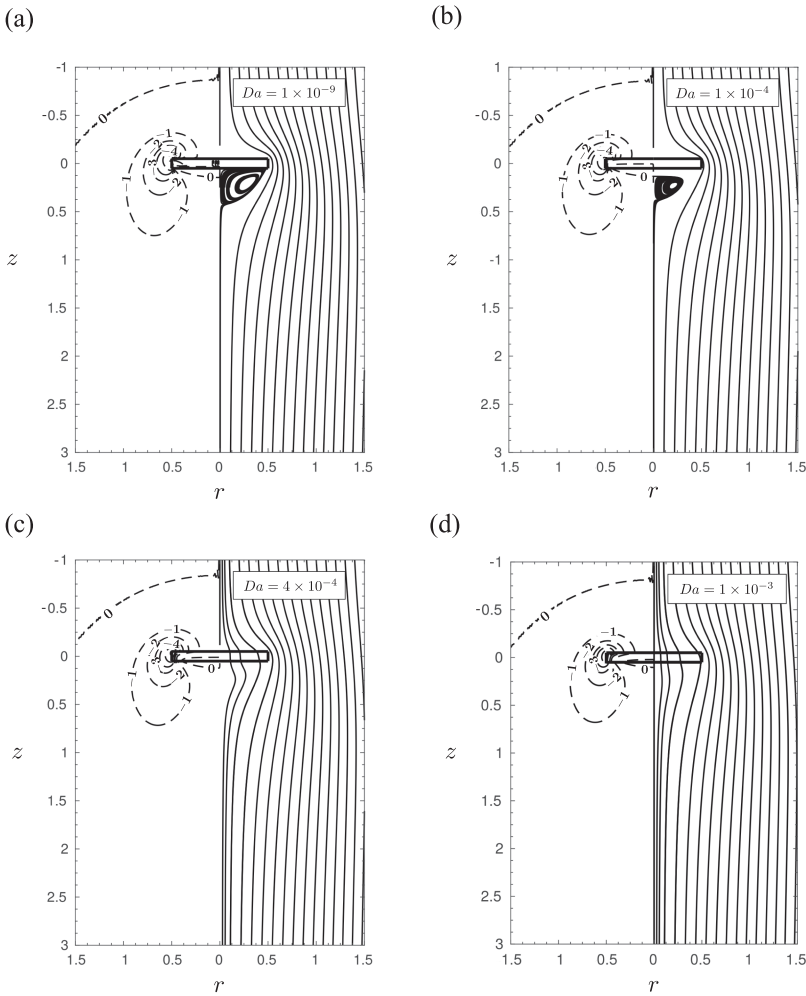
(a)

(b)

FIG. 2. Steady axisymmetric flow ($Re = 10$) with azimuthal vorticity (left panels; numbers indicate vorticity) and streamlines (right panel): (a) $Da = 10^{-9}$; (b) $Da = 10^{-4}$; (c) $Da = 4 \times 10^{-4}$; (d) $Da = 10^{-3}$.

(c)

(d)

as Da is increased, annihilating each other at $Da = Da_c$. The position of this bifurcation is examined in detail in Fig. 4(b), where Da_c is plotted against the corresponding Re. The critical Darcy number Da_c is not monotonically increasing in Re; it increases rapidly for low Re and reaches a global maximum $Da_{max} = 8.8 \times 10^{-4}$ for $Re = 44.4$ (indicated by a $\times$ at the turning point). Hence, Da_{max} represents the maximum Da a permeable disk can have, across all Re considered here, to maintain a recirculating vortex. For $Re > 44.4$, Da_c decreases uniformly as the highest $Re = 130$ is reached. The highly permeable regime occupies $Da \geq 10^{-3}$, which ensures that no wake is possible (i.e., $Da > Da_{max}$). The boundary between the wake and no wake regimes is given by the following equation:

$$Da_c(Re) = Da_{max} \exp\left[-c_1 \log^2\left(Re/Re_{max}\right)\right] \times \cdots$$

$$\times \exp\left[c_2 \left\{(Re/Re_{max})^2 - 2\log(Re/Re_{max}) - 1\right\}\right], \tag{8}$$

where $Da_{max} = 8.8 \times 10^{-4}$, $Re_{max} = 44.4$, and the best fit coefficients $c_{1,2}$ (and 95% confidence interval bounds) are $c_1 = 0.612 \pm 0.023$, $c_2 = 0.044 \pm 0.006$.

The collapse of the recirculating wake as Da approaches Da_c is shown in Figs. 5(a) and 5(b). Figure 5(b) shows that for fixed Da and fixed Re, there is precisely one possible wake

length L and that for a given Da, there are precisely two, one or zero critical Darcy numbers in the range $10 < Re < 130$. The wake length L for $Da = 10^{-9}$ is indistinguishable from that of an impervious disk except near $Re = 130$ [which is indicated by the dashed curve in Fig. 5(b)]. Figure 5(a) shows the rapid collapse of the recirculating wake as Da approaches Da_c from below. The distance $d = z_s - 1/(2\chi)$ downstream of the disk's downstream face where the recirculating wake first appears at $Da = Da_c$ is observed to increase with Re as follows: $d \propto Re^{0.89}$ in the range $10 < Re < 130$.

Away from Da_c, for Da approaching zero, the wake length approaches that of an impervious disk, so an effectively impervious regime exists corresponding to Da below which the wake length differs from its impervious disk counterpart by less than 1%; the value of Da that this occurs at for each of the curves is indicated by a solid black diamond in Fig. 4(a). To ensure that this is maintained across all Re considered in this study, the effectively impervious regime occupies $Da < 10^{-6}$.

In the case of high-permeability (i.e., Da tends to unity), the fluid moves through the permeable disk without appreciable deflection, and the drag coefficient of the permeable disk takes the following form (see Appendix B for details):

$$C_D = \frac{2}{\chi Da Re}. \tag{9}$$

(a)

(b)

(c)

(d)
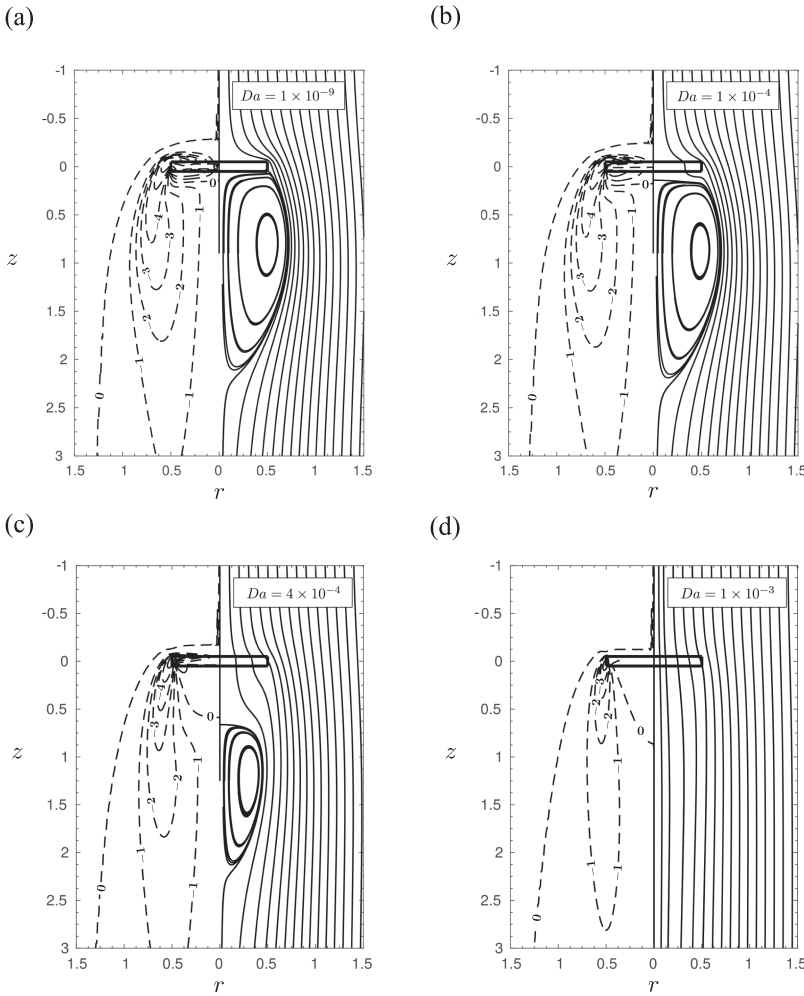

FIG. 3. Steady axisymmetric flow ($Re = 130$) with azimuthal vorticity (left panels; numbers indicate vorticity) and streamlines (right panel): (a) $Da = 10^{-9}$; (b) $Da = 10^{-4}$; (c) $Da = 4 \times 10^{-4}$; (d) $Da = 10^{-3}$.

The drag coefficient C_D is plotted in Fig. 6(a) as a function of Da for four Reynolds numbers: $Re = 10, 30, 44.4,$ and 130. Each curve is characterized by a local maximum in regime II and a high-permeability limit given by Eq. (9). The computed axial drag coefficient is compared with experimental data[15] for $Re = 10$–130 in Fig. 6(b).

Up to now, the dependence of C_D and L on Da and Re has been considered independently. Each quantity evolves in a qualitatively different manner as the parameters Re and Da are varied. The relative dependence of C_D and L on Da is now examined in order to explore if there are regions of the parameter space that are sensitive to one parameter but not the other. To do this, we select $Re = 130$, since at this value of Re, the peak in the drag coefficient differs most from its impervious-disk counterpart. This relative increase/decrease of both quantities is compared to that of an impervious disk over the entire range of Da considered in this paper. The ratio of C_D for a permeable disk to that of an impervious (solid) disk $C_{D,s}$ is shown in Fig. 7(a), and on the same graph, the ratio of the wake length L to that of an impervious disk L_s is also shown. Evidently, the wake length begins to fall off at a smaller Da than does C_D. At the boundary between regimes II and III, where the wake has disappeared, the drag coefficient is still about 70% of its impervious-disk value. In Fig. 7(b), we show that, at $Da = Da_c$, where there is no reverse flow, the drag coefficient differs from its impervious disk value by less than 5%. This indicates that the wake length can undergo large deviations from that of an impervious disk but that the drag is changed little at the same level of permeability. Hence, within regime II, there is scope to increase the permeability of the disk, resulting in a large decrease in the length or complete annihilation of the wake but with minimal effect on the drag.

IV. DISCUSSION

To date, to the authors' knowledge, the only study on the flow past permeable disks[13] is for $Re = 10^4$, and this prevents a quantitative comparison of our results to theirs from being carried out. However, we expect that the underlying physics in both cases is similar at both Re. To compare our results to theirs, we plot the pressure p and streamwise velocity u_z along the $r = 0$ axis at the highest Re considered in our study ($Re = 130$) in Fig. 8. We perform this for three values of Da, corresponding to regimes I, II, and II.

In regime I, the accumulation of vorticity due to the presence of the disk causes vortex formation directly behind the disk, as shown in Figs. 2(a) and 3(a). This picture is consistent with existing experiments on impervious disks; in Fig. 8(b), we show data from experiments[13] on impervious (×) and permeable (+) disks performed at $Re = 10^4$ alongside our results at $Re = 130$.
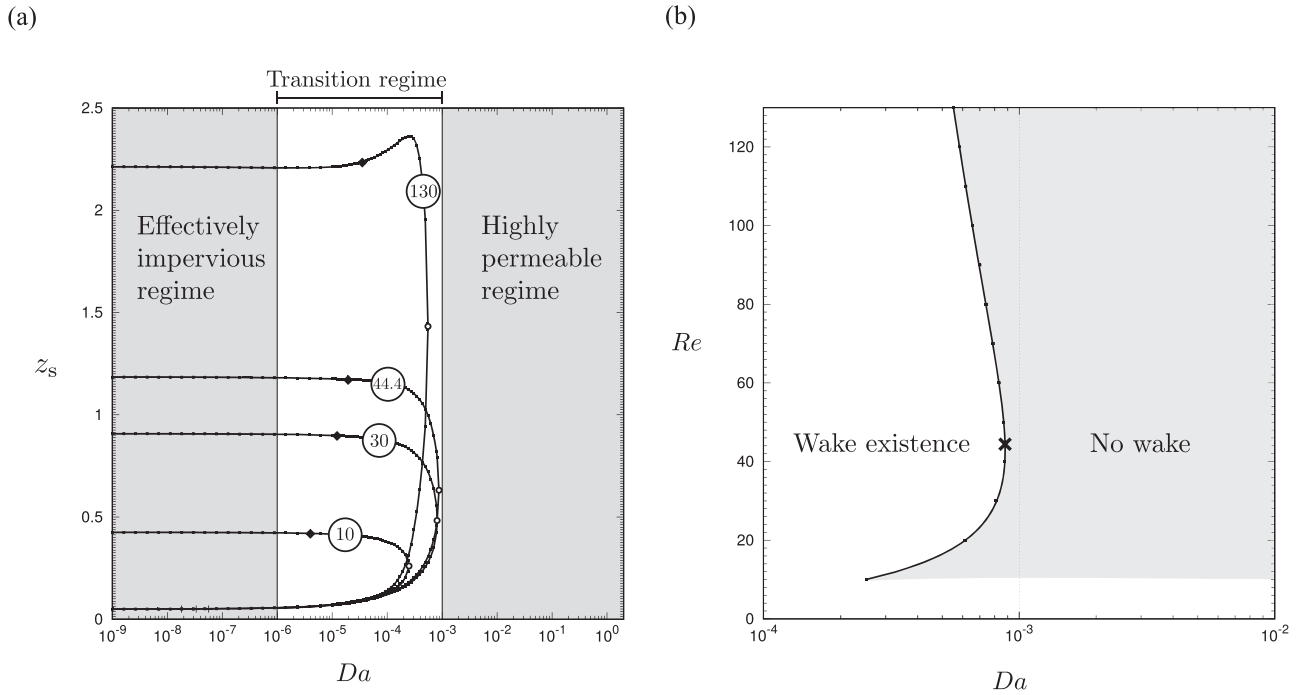
(a)

(b)

FIG. 4. (a) The position of the stagnation points (z_s) in the wake of a permeable disk as a function of Da; the circled numbers indicate Re of the flow. The bifurcation point, corresponding to the collapse of the wake, is indicated by the small annulus. The black diamonds indicate the point at which the difference between the wake length L and L_s is less than 1%. Each mark shows the computed value, and the solid line indicates the linear fit of these values. (b) The bifurcation diagram in the Re-Da plane (each point on the curve denotes the value of Da_c at the given Re) with the turning point at ($Da_{max} = 8.8 \times 10^{-4}$, 44.4) indicated by an ×.

The case of a permeable disk in regime II is different: the region of recirculating flow is not directly downstream of the disk as shown in Figs. 2(b) and 3(b), but is separated some distance downstream of the disk. Comparing Figs. 3(a)–3(c), the vortex is both smaller in width and length; the latter

is established precisely in Fig. 4(a) in good agreement with experiments on permeable plates.[22] In addition, the maximum reverse flow speed along the $r = 0$ axis is smaller for a permeable disk than it is for an impervious one, as shown in Fig. 8(b), in good agreement with experiments[13] on impervious
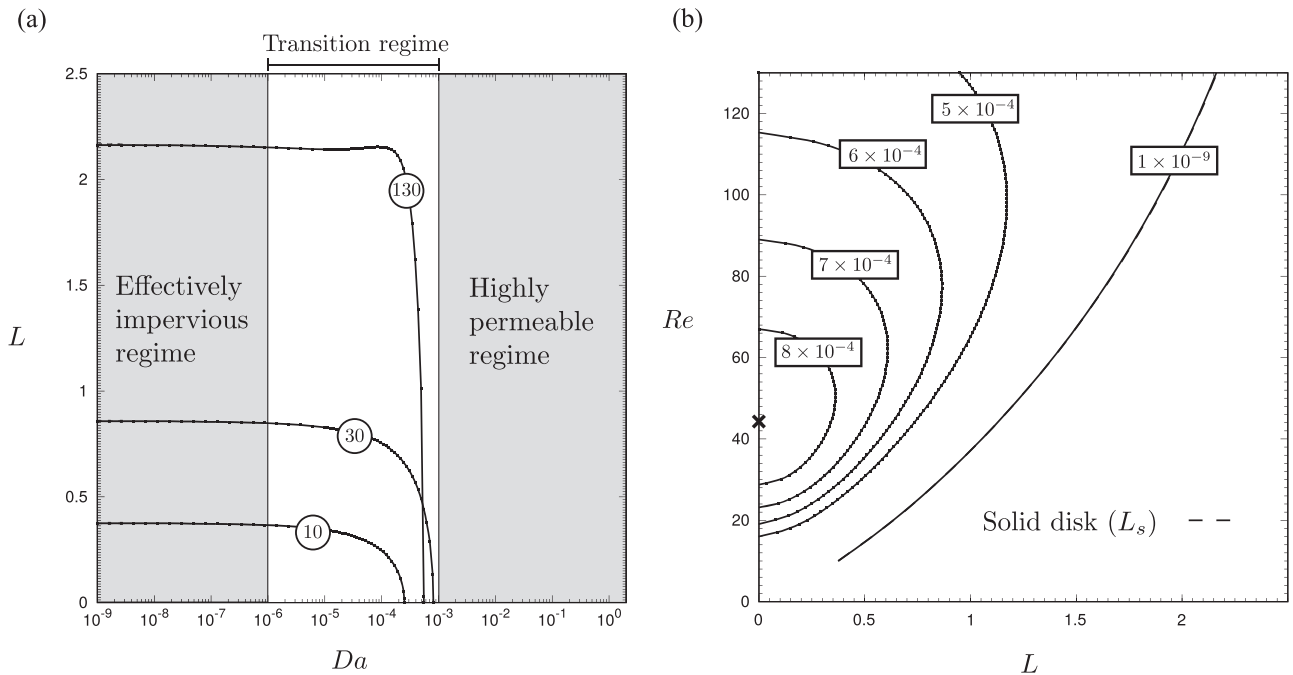
(a)

(b)

FIG. 5. (a) The wake length (L) behind a permeable disk as a function of Da; the circled numbers indicate Re of the flow. (b) The collapse of the wake as $Da \to Da_{max} = 8.8 \times 10^{-4}$ and $Re \to 44.4$ (indicated by an ×); the boxed numbers indicate Da of the disk.

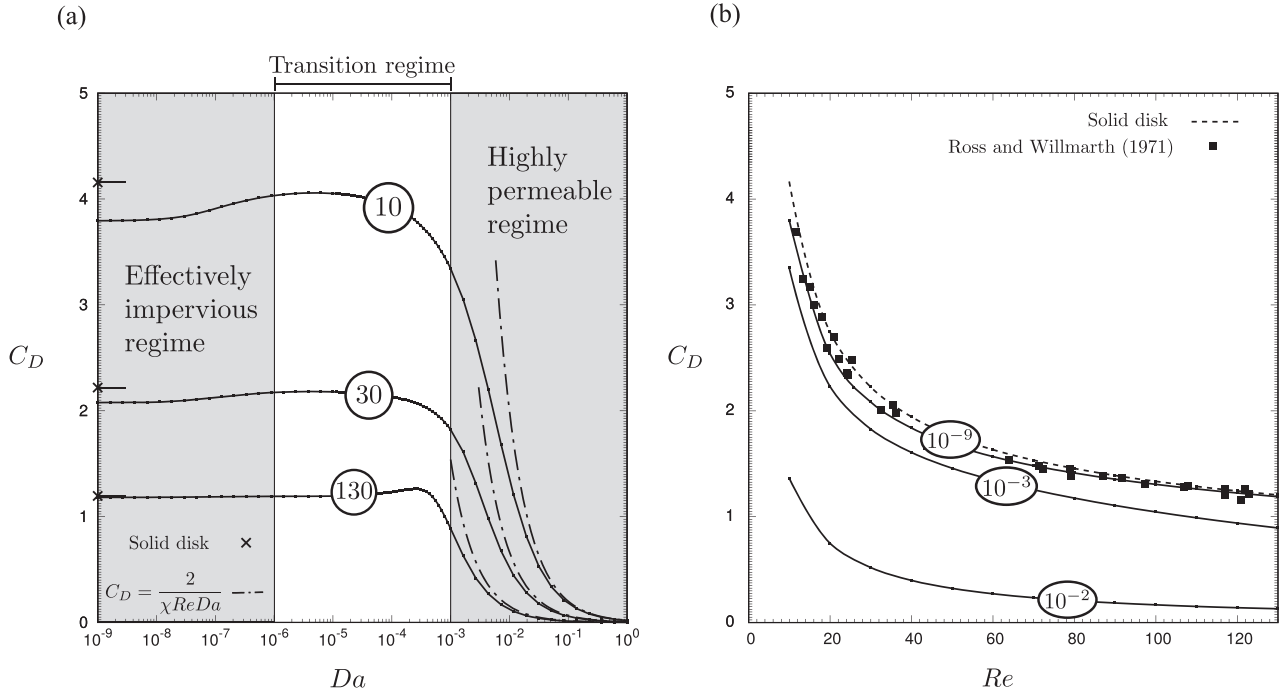(a)   (b)

FIG. 6. The drag coefficient C_D for a permeable disk: (a) as a function of Da, with circled numbers indicating Re of the flow, and (b) as a function of Re with circled numbers indicating Da of the disk. The black squares are experimental[15] data points for the drag coefficient of an impervious disk. The high-permeability approximations are indicated by the $-\cdot-$ curves, which are given by Eq. (9).

and permeable disks, which are also included in Fig. 8(b). The permeability of the permeable disk used in these experiments was not measured, so we have calculated the nominal Darcy number for their experiments to be $Da = 3.75 \times 10^{-5}$, based on an application of the Carman-Kozeny equation.[28,29]

We find that disks in regime I have larger maximum reverse flows along the $r = 0$ axis than those in regime II and that the rate of velocity recovery for disks in regime I is faster than disks in regime II/III, as shown in Fig. 8(b). Due to the fluid bleed through the disk in regime II, the entrainment

(a)   (b)
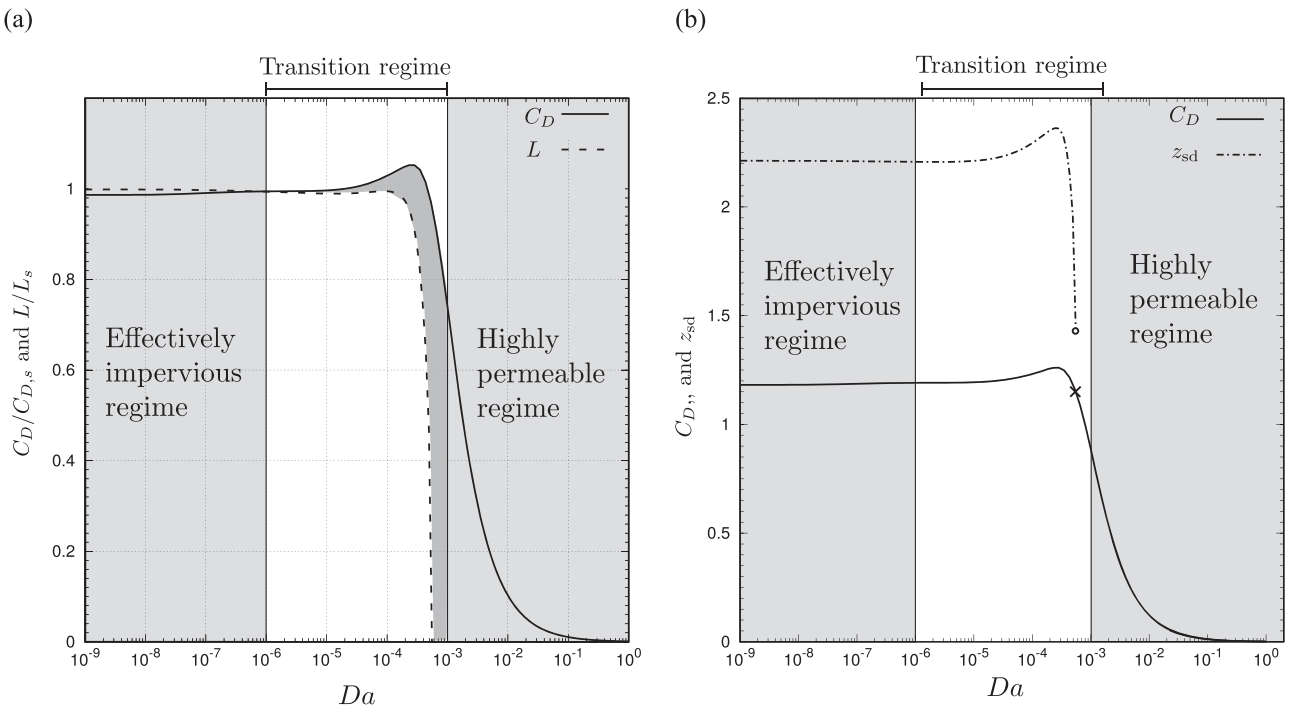
FIG. 7. (a) The increase in the drag coefficient C_D and wake length L for a permeable disk as a function of Da compared to that of an impervious disk for $Re = 130$. (b) The drag coefficient C_D and the position of the downstream stagnation point z_{sd}, showing the value of drag coefficient at $Da = Da_c = 5.51 \times 10^{-4}$ (indicated by an $\times$; $C_D = 1.15$) and the bifurcation point (indicated by an annulus; $z_{sd} = 1.43$).
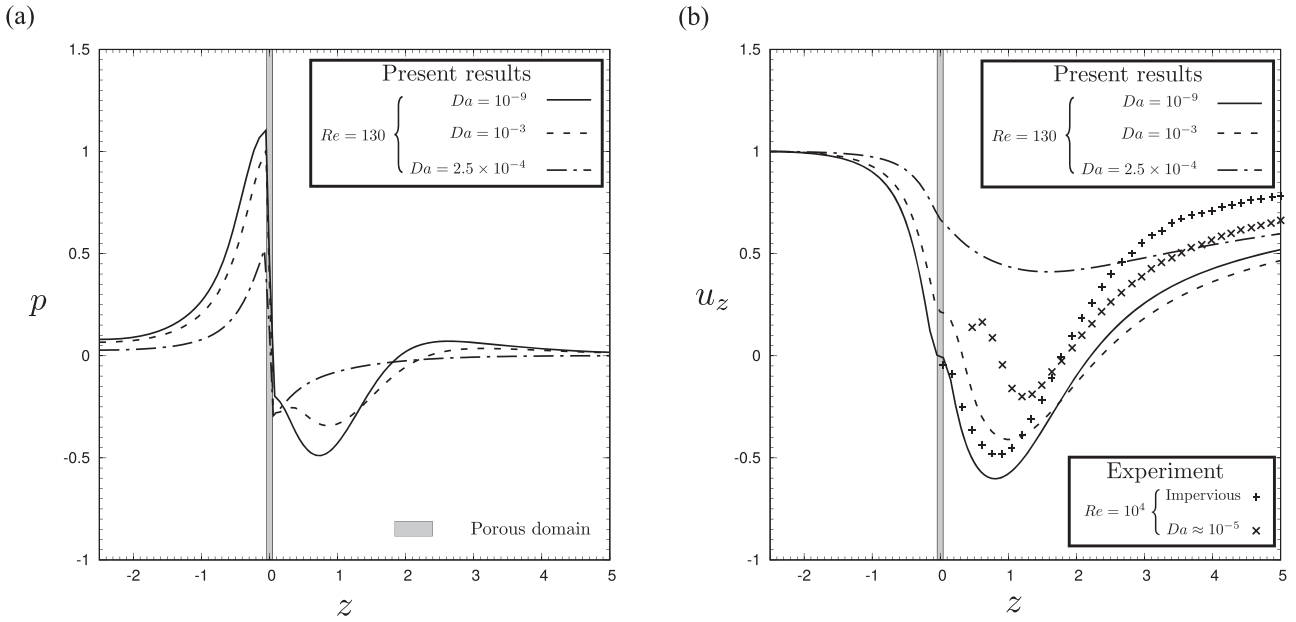
(a)

(b)

FIG. 8. (a) The pressure p along the $r = 0$ axis for $Re = 130$ and three values of $Da = 10^{-9}$, 2.5×10^{-4}, and 10^{-3}, corresponding to regimes I, II, and III, respectively. (b) The axial velocity u_z along the $r = 0$ axis for $Re = 130$ and Da as in (a). The experimental data in (b) are redrawn from Fig. 5(a) of Ref. 13.

of the shear layer is significantly reduced and the position of the downstream stagnation point z_{sd} increases. These observations are consistent with experimental measurements,[13] which are shown alongside our results in Fig. 8(b). These experiments show that the position of the downstream stagnation point is further downstream than the stagnation point of the wake behind an equivalent impervious disk, in excellent agreement with our findings in Fig. 4(a), which show a maximal downstream excursion of the downstream stagnation point at intermediate Da for the highest Re considered. The transverse velocity profiles of the wake region are presented in Fig. 9. In

Fig. 9(b), we have plotted the experimental[13] measurements of u_z along the radial direction at a distance of one disk diameter downstream of the disk's rear face at $Re = 10^4$. In our simulations and in experiment, the maximum reverse flow along the axis and the velocity recovery are shown to decrease with increasing Da.

We also remark that our velocity profiles are in good agreement with the experiments on the flow around permeable plates.[22] Consistent with our results, a reversed flow bubble detaches and moves downstream. The downstream stagnation point undergoes a maximal excursion from the plate, in

(a)

(b)
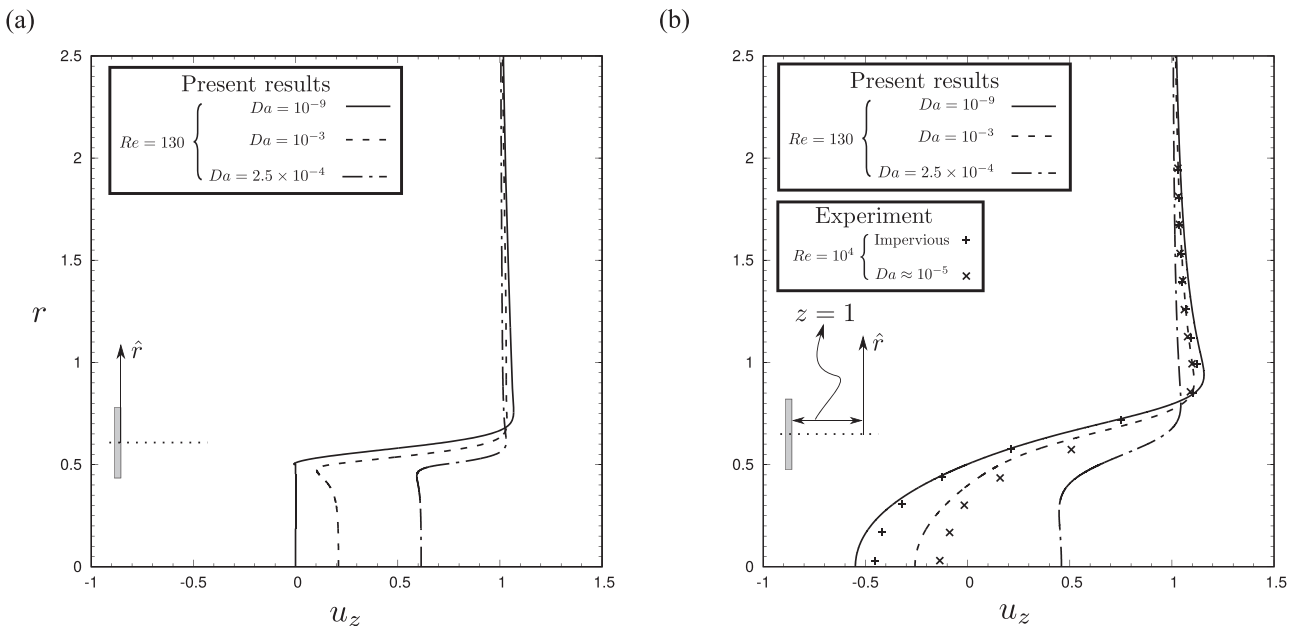

FIG. 9. The streamwise velocity u_z profiles across the wake for an axial position z: (a) on the disk's face and (b) a distance of one disk diameter downstream of the disk's rear face, for three values of $Da = 10^{-9}$, 2.5×10^{-4}, and 10^{-3}, corresponding to regimes I, II, and III, respectively. The experimental data in (b) are redrawn from Figs. 6(a) and 6(b) of Ref. 13.

agreement with our results in Fig. 4(a). The experiments show that there are two flow regimes,[22] one corresponding to high permeability and one to low permeability, and that the transition between the two flow regimes is quite sudden. This is in good agreement with our findings: we have two distinct regimes corresponding to low and high values of permeability (regimes I and III), whereas the abrupt changes in wake topology behind a permeable plate[22] correspond to the bifurcation points in regime II, which show rapid destruction of the wake.

The presence of the global maximum in C_D in Fig. 6(a) has been found in previous experimental and numerical studies,[3,4,11] but what causes this increase remains unclear. To understand what causes this increase, consider the case of a highly permeable disk (far to the right of regime III); in this case, the velocity is constant and axial, the pressure field is antisymmetric across the disk, and according to Eq. (9), C_D increases inversely with Da. However, this trend cannot continue indefinitely as Da approaches 0; as we approach regime II from the right, the assumption of $\partial p/\partial z = 0$ breaks down, and Eq. (9) is no longer valid. In fact, the pressure behind the disk is lower than it is in the far field due to the pressure loss across the permeable disk. While, far downstream, the pressure must have risen to the level of the freestream pressure. Decreasing Da within regime III causes the axial velocity u_z at some point located a short distance downstream of the disk to decrease in the streamwise direction driven by the positive pressure gradient there [as can be seen in Fig. 8(b)]. Within regime III, the viscous contribution to the z-component of Eq. (4) is negligible, and along the disk's axis, we have a balance of the pressure gradient and the inertial terms,

$$\frac{\partial p}{\partial z} = -u_z \frac{\partial u_z}{\partial z}, \tag{10}$$

which, when integrated with respect to z, gives the Bernoulli equation. Note that the right-hand side of Eq. (10), by the above reasoning, must be positive. This inviscid effect can only dampen the increase of Δp across the disk and thus the increase of C_D with decreasing Da; it cannot reverse the trend, and this effect cannot account for reversal of the flow.

However, as the steepness of the velocity gradients overcomes the smallness of $1/Re$ in Eq. (4), this picture begins to break down and Eq. (10) is no longer valid. Instead, we can no longer neglect the influence of viscosity in the wake region, and we must include the viscous contribution. Hence, along the disk's axis, u_z and p satisfy

$$\frac{\partial p}{\partial z} = -u_z \frac{\partial u_z}{\partial z} + \frac{1}{Re}\left\{\frac{\partial^2 u_z}{\partial r^2} + \frac{\partial^2 u_z}{\partial z^2}\right\}. \tag{11}$$

Observe that the inertial term on the right-hand side of Eq. (11) is non-negative as shown above but that the viscous term must be negative near to the disk, as shown in Figs. 9(a) and 8(b). Hence, as the velocity gradient increases with Da, eventually the viscous effects balance the inertial effects, and the right-hand side of Eq. (11) vanishes. As the gradients become steeper still, the viscous effects dominate, and the pressure gradient becomes negative, according to Eq. (11). This transition from
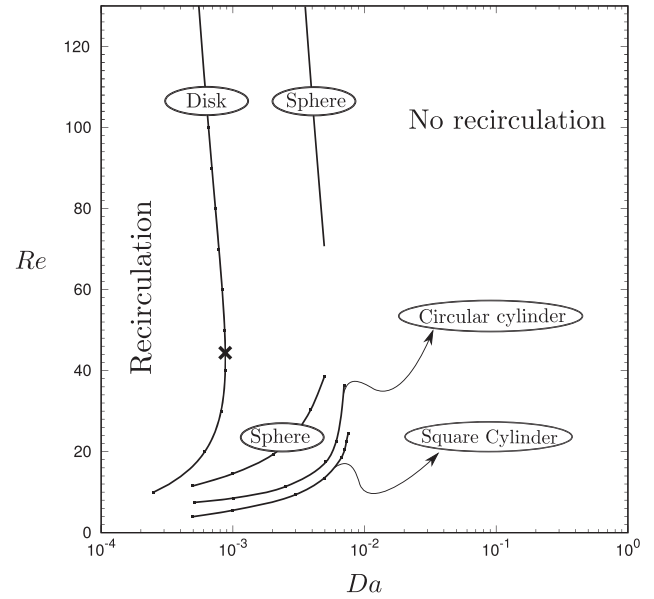

FIG. 10. The bifurcation diagram for a permeable disk (present results; global bifurcation indicated by an ×), for a permeable sphere,[8] for a permeable square,[6] and a circular cylinder,[7] in the Re-Da plane.

positive to negative pressure gradient as we move from regime III through regime II to regime I is shown in Fig. 8(a) for $Re = 130$.

This effect is restricted to the wake region, whereas the sign of the pressure gradient on the disk's front is positive throughout this process. The pressure experiences a slower rate of increase on the rear face compared with the front face as Da is decreased [as shown in Fig. 8(a)] reflecting the competition between the viscous effects and the inertial effects in the wake. This widening of Δp leads to a local maximum in the value of C_D, before gradually approaching that of an impervious disk as $Da \to 0$. At high permeabilities, the pressure gradient is balanced by inertial effects, whereas at low permeabilities, the pressure gradient is balanced by viscous effects. Hence, one may consider another classification for the boundary between regimes I and II which is based on the sign/magnitude of the pressure gradient and inertial terms in Eq. (11), on the disk's rear face.

Within a narrow interval of Da, C_D does not change appreciably, yet the wake length L drops rapidly from its maximum value to zero [Figs. 7(b) and 8(a)]. For an impervious and permeable disk of the same physical dimensions, the recirculating region behind the latter can be reduced or eliminated choosing different values of Da. This resembles a base bleed effect and suggests that Da can be used as a flow control parameter in the movement of permeable disks through a viscous fluid.

At higher Re than considered here, it can be speculated that this flow control mechanism could be useful to control or suppress the vortex shedding behind impervious bodies.[30] This would have important implications for the dynamics of freely falling impervious disks. Perhaps a disk's permeability can be tuned to control the dynamics of the disks. Furthermore, this control may not come at the expense of a significant loss in the disk's C_D; in fact, it may lead to an *increase* in C_D. This is of particular relevance in the design of drag-enhancing

parachutes, which aim to optimize drag and control at the same time.

We have considered the case of a permeable disk, and we find that there is a curve in the *Re-Da* parameter space that divides the regime where the disk has a recirculating wake from the regime where the disk does not have one. Similar curves have been found for different geometries, such as the 2D square cylinder,[6] 2D circular cylinder,[7] and a sphere.[8] We present our results for the permeable disk alongside the results for other geometries in Fig. 10. We note that previous studies on square and circular cylinders were restricted to a smaller range of *Re*, within which no turning point in the *Re-Da* space was observed. One study, for the permeable sphere,[8] however, considered a wider range of *Re* and indeed observed a turning point. Interestingly, this turning point occurs at a *Re* close to that for a disk.

V. CONCLUSIONS

We have examined the viscous flow over a permeable circular disk of aspect ratio $\chi = 10$ in the Reynolds number (*Re*) range of 10–130 and in the Darcy number (*Da*) range of 10^{-9} to 1. We observed three flow regimes: (I) an effectively impervious regime existed when $Da < 10^{-6}$, characterized by the presence of a toroidal vortex located a very short distance downstream of the disk; (II) a transition regime when $10^{-6} < Da < 10^{-3}$ where the lower vorticity production weakens the vortex in regime I, causing the toroidal vortex to shorten and move downstream, eventually vanishing completely; (III) a highly permeable regime, in which there is no recirculating wake.

We have calculated the limiting permeability of a permeable disk $Da_{\max}$ above which no recirculation can occur [regime III; Figs. 5(a) and 5(b)]. The presence of such an upper limit is consistent with the results for other bodies,[6–8] but the upper limit has never been computed in any of these studies. For *Da* greater than this limiting permeability, we show that the drag coefficient, C_D, depends on *Re*, *Da*, and χ and asymptotically approaches zero as permeability increases, consistent with the tendency of permeable spheres and cylinders.[4,21]

In regime II, the drag coefficient is characterized by a local maximum close to the boundary between regime II and regime III [Fig. 6(a)], which is consistent with the experimental results for permeable spheres, cylinders, and other permeable bodies.[3,4,11] The peak in C_D occurs at higher *Da* for decreasing *Re*, and the peak value significantly exceeds the drag on an impervious disk of the same dimensions $C_{D,s}$ for moderate values of *Re*. This finding is consistent with the numerical simulations and experiments on the flow past permeable cylinders,[4] where increases were found for moderate-*Re* flow past a permeable cylinder compared with an impervious one.

The wake length L tends asymptotically to its impervious-disk counterpart L_s as *Da* is decreased to zero: in regime I, *L* is within 1% of its impervious-disk value (Fig. 5). In regime II, we find that both stagnation points generally move downstream as the wake shortens, with the downstream stagnation point uniformly decreasing from its impervious-disk value, before rapidly approaching the upstream stagnation point as $Da \rightarrow Da_c$ [Fig. 4(a)]. We also find that for higher *Re* (*Re* = 130,

for example), the downstream stagnation point undergoes an small downstream excursion characterized by a local maximum in its position close to the boundary between regime II and III, which is consistent with experiments on permeable disks and plates.[13,22]

We compare the relative dependence of C_D and *L* on *Da* [Fig. 7(a)], showing that the wake length can undergo large deviations from its impervious-disk value, but with minimal change in the drag coefficient over the same range. This suggests that permeability could be used as an effective flow control mechanism in the motion of permeable bodies. The wake behind an impervious disk at *Re* considered in this study, $10 < Re < 130$, is steady; at higher *Re*, the flow past impervious disks is generally unsteady with a loss in symmetry. Hence, to explore higher *Re*, the assumptions of axisymmetry and steady-state in the current model must be relaxed—this is left as future work.

ACKNOWLEDGMENTS

APPENDIX A: UNCERTAINTY ANALYSIS

We performed the verification and validation of *L* and C_D computed with COMSOL Multiphysics. We considered the case of a permeable disk with very low permeability ($Da = 10^{-25}$) and an impervious disk for the minimum (*Re* = 10) and maximum (*Re* = 130) Reynolds numbers examined in the paper, for which some experimental data are available in the literature.

1. Verification

The numerical uncertainty U_{num} is quantified using the method proposed by Viola, Bot, and Riotte.[31] This method was initially developed for yacht sail aerodynamics, but it can be applied to any other application. The method is as follows: the 95% confidence interval of any computed value ϕ_{num} (in this paper, ϕ_{num} is either *L* or C_D) is given by $\phi_{\mathrm{num}} \pm U_{\mathrm{num}}\phi_{\mathrm{num}}$, where the numerical uncertainty U_{num} is the sum of the uncertainties due to the grid (U_g) and the iterative convergence (U_c),

$$U_{\mathrm{num}} = U_g + U_c.$$

To compute U_g, simulations with $n_g = 6$ different grid sizes (*N* cells in the radial direction and *M* cells in the axial direction) were performed. The grid sizes ($N \times M$) of grids 1-6 are shown in the second column of Table I. The reference grid, for which the uncertainty is computed, can be either uniformly refined or uniformly coarsened using a structured refinement strategy. We define the relative step size h_i as the ratio of the cell sizes of the *i*th grid to that of the reference grid (our reference grid is always grid 6, and $h_{i+1} = h_i/\sqrt{2}$) and ϕ_i as the ratio of the quantity (either *L* or C_D) computed with the *i*th grid to that computed with the reference grid.

As *h* approaches zero, the fit of ϕ_i should converge to $\phi = \phi_0$ with the order *p* of the adopted numerical scheme. Given that different schemes are used to solve the coupled

TABLE I. The uncertainty in the numerical method due to the grid (U_{num}; expressed as a percentage of ϕ_{num}) for the drag coefficient C_D and the length of the wake L for a highly impermeable disk ($Da = 1 \times 10^{-25}$).

		$Re = 10$		$Re = 130$	
Grid	$N \times M$	U_{C_D} (%)	U_L (%)	U_{C_D} (%)	U_L (%)
1	68×357	2.94	1.22	0.82	0.21
2	96×504	2.18	0.78	0.65	0.26
3	136×714	1.59	0.49	0.51	0.25
4	192×1008	1.15	0.30	0.39	0.24
5	272×1428	0.81	0.19	0.28	0.23
6	384×2016	0.56	0.13	0.20	0.22

TABLE II. The uncertainty in the numerical method due to the grid (U_{num}; expressed as a percentage of ϕ_{num}) for the drag coefficient $C_{D,s}$ and the length of the wake L_s for an impervious disk.

		$Re = 10$		$Re = 130$	
Grid[a]	$N \times M$	$U_{C_{D,s}}$ (%)	$U_{L,s}$ (%)	$U_{C_{D,s}}$ (%)	$U_{L,s}$ (%)
1	68×357	3.50	1.13	0.41	0.83
2	96×504	2.72	0.70	0.39	0.66
3	136×714	2.07	0.42	0.35	0.50
4	192×1008	1.56	0.25	0.29	0.36
5	272×1428	1.15	0.16	0.23	0.27
6	384×2016	0.82	0.10	0.15	0.20

[a]The grids used for the impervious disk computations are identical to those used for the permeable disk, except that the permeable region is absent.

system of equations, p is generally unknown. Therefore, a curve,

$$\phi(h) = \phi_0 + \alpha h^p,$$

is fitted through the set of ϕ_i. The parameters $\{\phi_0, \alpha, p\}$ can be estimated by a least squares method. We also compute the standard error of the fit,

$$\sigma_{\mathrm{fit}} = \sqrt{\frac{\sum_{i=1}^{n_g} (\phi_i - \phi(h_i))^2}{n}},$$

where $\phi(h_i)$ is the value of the function ϕ evaluated at h_i and $n = n_g - 3$ is the number of degrees of freedom of the fit. The extrapolated value ϕ_0 is the expected value of ϕ for an infinitely fine grid. This allows estimating the error of the reference grid as

$$\delta = |1 - \phi_0|,$$

hence the grid uncertainty is then given by

$$U_g = 1.25\delta + \sigma_{\mathrm{fit}},$$

where 1.25 is a safety factor.[32] In all of our computations, the iterative error on the value of C_D is specified by the solver's relative tolerance, which was set to 10^{-9} in all computations; since this is several orders of magnitude smaller than U_g, we neglect it for both C_D and L. The results from our uncertainty analysis for the numerical error are presented in Table I, where U_{C_D} and U_L are the uncertainties due to the numerical method for C_D and L, respectively. The results presented in Sec. III are obtained from simulations performed on grid 6; hence, we find that $U_{\mathrm{num}} < 1\%$ in value for C_D and L at the lowest and highest Re considered in this study.

The small numerical uncertainties U_{num} in Table I give us confidence in the presented trends of C_D and L with Re and Da. In order to validate the solution, however, we must compare with experimental measurements of C_D and L. To the authors' knowledge, however, there are no experimental measurements of C_D or L for permeable disks in the literature; hence, we seek to validate our model by considering the drag coefficient and wake of an impervious disk:[15] denoted as $C_{D,s}$ and L_s, respectively. We begin by computing U_{num} in $C_{D,s}$ and L_s for grids 1-6 as we did in Table I: our results are presented in Table II. We find that U_{num} in $C_{D,s}$ and L_s is the same order of magnitude as for a permeable disk.

2. Validation

For validation purposes, we use the experimental data for an impervious disk.[15] We consider the uncertainty in the drag coefficient $C_{D,s}$. The first two rows in Table III show the computed value ϕ_{num} and the associated numerical uncertainty U_{num}, taken from the last row of Table II. The second and third rows are the measured values ϕ_{exp} at $Re = 10$ and $Re = 130$, which are obtained using a best-fit curve through the experimental measurements. The uncertainty due to the experimental measurements was not presented in Ref. 15, hence we estimate U_{exp} to be the 95% confidence interval of the mean of the technical repeats conducted nearest $Re = 10$ and $Re = 130$ in Ref. 15, respectively. The fifth row in Table III shows the validation uncertainty $U_{\mathrm{val}} = \sqrt{U_{\mathrm{num}}^2 + U_{\mathrm{exp}}^2}$ and the sixth row shows the error $\mathcal{E} = \phi_{\mathrm{num}} - \phi_{\mathrm{exp}}$ in the estimate of the drag coefficient.

Our analysis reveals that our numerical simulations overpredict $C_{D,s}$ by 5.85% and 2.56% for $Re = 10$ and $Re = 130$, respectively, compared with experiment. In the latter case ($Re = 130$), mod $|\mathcal{E}| < U_{\mathrm{val}}$, and hence our results are validated at a level of 4.31% for $Re = 130$. However, in the former case ($Re = 10$), mod $|\mathcal{E}| > U_{\mathrm{val}}$, so our simulations are not validated for $Re = 10$. Since $\mathcal{E} > 0$, the associated modeling error for the drag coefficient $\delta_{\mathrm{mod},C_D}$ is also positive.

To find the main source of this modeling error, we compute the error introduced by choosing a finite domain size. In order to calculate this error, we select $n_{\mathrm{mod}} = 4$ domains sizes: A-D with radial extent W and axial extent H (as shown

TABLE III. Summary of the uncertainty due to the numerical method and the experimental data in the drag coefficient $C_{D,s}$ for an impervious disk.

	$Re = 10$ $C_{D,s}$	$Re = 130$ $C_{D,s}$
ϕ_{num}	4.16	1.20
U_{num} (%)	0.82	0.15
ϕ_{exp}	3.93	1.17
U_{exp} (%)	4.08	4.31
U_{val} (%)	4.17	4.31
$\mathcal{E} = \phi_{\mathrm{num}} - \phi_{\mathrm{exp}}$	+0.23	+0.03
$\mathcal{E}$ (%)	+5.85	+2.56

TABLE IV. The modeling error δ_{mod} in the mathematical model due to the finite-sized domain for the drag coefficient $C_{D,s}$ and the length of the wake L_s for an impervious disk. The values for the width W and height H refer to the radial and axial extent of the domain in disk diameters, respectively. All computations are performed on grid 6: see Table I.

		Re = 10		*Re* = 130	
Domain	$W \times H$	$\delta_{\mathrm{mod},C_{D,s}}$ (%)	$\delta_{\mathrm{mod},L,s}$ (%)	$\delta_{\mathrm{mod},C_{D,s}}$ (%)	$\delta_{\mathrm{mod},L,s}$ (%)
A	4.2×12.4	+4.92	+0.16	+0.68	−0.04
B	6.0×17.5	+3.82	+0.07	+0.66	−0.03
C	8.5×24.8	+3.08	+0.03	+0.47	−0.01
D	12.0×35.0	+2.35	+0.03	+0.07	−0.00

TABLE V. The modeling error δ_{mod} in the mathematical model due to the finite-sized domain for the drag coefficient C_D and the length of the wake L for a highly impermeable disk. The values for the width W and height H refer to the radial and axial extent of the domain in disk diameters, respectively. All computations are performed on grid 6: see Table I.

		Re = 10		*Re* = 130	
Domain	$W \times H$	$\delta_{\mathrm{mod},C_D}$ (%)	$\delta_{\mathrm{mod},L}$ (%)	$\delta_{\mathrm{mod},C_D}$ (%)	$\delta_{\mathrm{mod},L}$ (%)
A	4.2×12.4	+3.38	+0.14	+1.20	+0.02
B	6.0×17.5	+1.22	+0.06	+0.43	+0.00
C	8.5×24.8	+0.40	+0.02	+0.22	+0.00
D	12.0×35.0	+0.17	+0.02	+0.18	+0.00

in Table IV). We obtain the solution within each domain, using the same grid, and compute $C_{D,s}$ and L_s in each case. We define the relative domain size W_{ref}/W_i as the ratio of the width of the reference domain (our reference domain is domain B) to the width of the ith domain and $\phi_i = C_{D,s}/C_{D,s\,\mathrm{ref}}$ as the ratio of ϕ computed in the ith domain to ϕ computed in the reference domain. As W_{ref}/W_i approaches zero, the fit of ϕ_i should converge to $\phi = \phi_0$, which approximates the value obtained using an infinite domain. We obtain the value for ϕ_0 by fitting a curve through the obtained data using a similar method outlined in Appendix A 1. The error introduced due to the choice of finite domain is then calculated using

$$\delta_{\mathrm{mod},\phi} = 1 - \phi_0.$$

The results of this study are summarized in Table IV. We note that the modeling error is typically positive and smaller than 1% for all computed quantities on domain B (the domain used in the main body of this paper). However, for low *Re*, the magnitude of this error rises to over 3% for $C_{D,s}$. Note that the sign of this error is positive for $C_{D,s}$, meaning that our simulation results are always an overestimate of the true result. This is consistent with our validation results above, which showed that the solution was validated at *Re* = 130 but not at *Re* = 10 and that the modeling error was approximately $\mathcal{E} \pm U_{\mathrm{val}} = 5.85\% \pm 4.17\%$. Hence, we identify that the main source of the modeling error for *Re* = 10 is the finite size of the domain.

In order to check that the modeling errors are the same order of magnitude for C_D as they are for $C_{D,s}$, we follow the same procedure as described above, but for the case of a permeable disk. The error due to the use of a finite domain size

for permeable disks is summarized in Table V, where we find that the errors are of the same order of magnitude as found for $C_{D,s}$; we note that the error in C_D and $C_{D,s}$ at low *Re* is consistently higher than at higher *Re* and that the error in $C_{D,s}$ is significantly higher than the error in C_D at *Re* = 10. A plot of the error in $\phi_i = C_D/C_{D\mathrm{ref}}$ (for *Re* = 10) versus relative domain size for grid 6 is shown in Fig. 11, where W_{ref}/W_i is the ratio of the width of the reference domain (domain B) to the width of the ith domain.
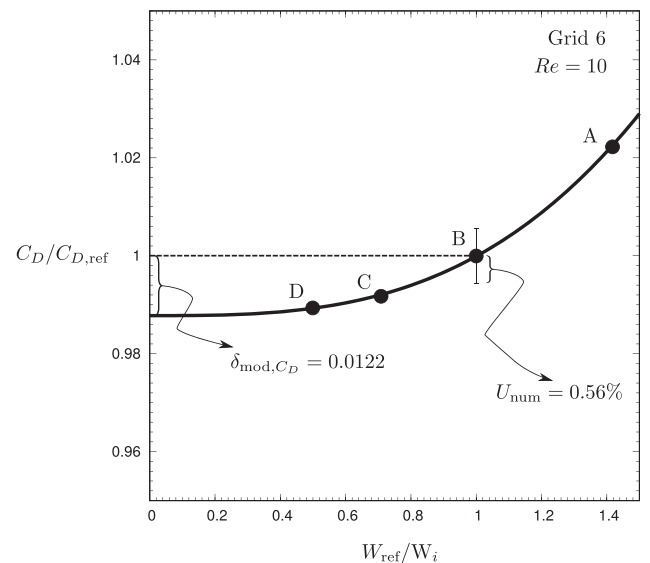

FIG. 11. The convergence of $\phi = C_D$ (for *Re* = 10) as the size of the domain is increased. The modeling error due to the finite grid is indicated by $\delta_{\mathrm{mod},C_D}$. The error bars indicate the numerical uncertainty, U_{num}, at a 95% confidence level in C_D (see Table I).

APPENDIX B: DERIVATION OF EQ. (9)

In the absence of a permeable disk, the velocity field is its freestream value throughout the domain. In the highly permeable regime, we expand $\mathbf{u}$ and p in an asymptotic series, in which the small parameter $\gamma \ll 1$ is a measure of the deviation of the flow from uniform flow,

$$\mathbf{u} = \mathbf{u}^{(0)} + \gamma \mathbf{u}^{(1)}(r,z) + \mathcal{O}\left(\gamma^2\right), \tag{B1}$$

$$p = p^{(0)}(r,z) + \gamma p^{(1)}(r,z) + \mathcal{O}\left(\gamma^2\right), \tag{B2}$$

where $\mathbf{u}^{(i)}$ and $p^{(i)}$ are $\mathcal{O}(1)$, $\gamma \ll 1$, and $\mathbf{u}^{(0)}$ is the leading-order uniform flow. We insert the expansions (B1) and (B2) into (4) and (5), which yields

$$\nabla p^{(0)}(r,z) = 0, \tag{B3}$$

in the fluid domain, and

$$0 = -\nabla p^{(0)}(r,z) - \frac{1}{Da}\frac{1}{Re}\mathbf{u}^{(0)}, \tag{B4}$$

in the porous region, at leading order $\mathcal{O}(1)$, respectively. To satisfy the boundary condition at the inlet ($\mathbf{u} = \hat{z}$), the velocity field must satisfy $\mathbf{u}^{(0)} = \hat{z}$ throughout the fluid domain. By continuity of the velocity and pressure fields across the porous/fluid interface, we find that the leading-order contribution to the pressure satisfies

$$\nabla p^{(0)}(r,z) = -\frac{1}{Da}\frac{1}{Re}\hat{z}, \tag{B5}$$

in the porous region. The difference in pressure between the upstream and downstream face Δp is then approximated by

$$\Delta p^{(0)} = \frac{1}{\chi Da}\frac{1}{Re}, \tag{B6}$$

hence the drag coefficient is given by

$$C_D = 2\Delta p^{(0)},$$

and the resulting expression, Eq. (9), follows. Similar equations to Eq. (9) have been derived for a 2D circular cylinder[4] and a permeable sphere.[21]

[1]M. Le Bars and M. G. Worster, "Interfacial conditions between a pure fluid and a porous medium: Implications for binary alloy solidification," J. Fluid Mech. **550**, 149–173 (2006).

[2]P. Yu, T. S. Lee, Y. Zeng, and H. T. Low, "Fluid dynamics and oxygen transport in a micro-bioreactor with a tissue engineering scaffold," Int. J. Heat Mass Transfer **52**, 316–327 (2009).

[3]J. H. Masliyah and M. Polikar, "Terminal velocity of porous spheres," Can. J. Chem. Eng. **58**, 299–302 (1980).

[4]P. D. Noymer, L. R. Glicksman, and A. Devendran, "Drag on a permeable cylinder in steady flow at moderate Reynolds numbers," Chem. Eng. Sci. **53**, 2859–2869 (1998).

[5]V. Casseau, G. De Croon, D. Izzo, and C. Pandolfi, "Morphologic and aerodynamic considerations regarding the plumed seeds of tragopogon pratensis and their implications for seed dispersal," PLoS One **10**, e0125040 (2015).

[6]P. Yu, Y. Zeng, T. Lee, H. Bai, and H. Low, "Wake structure for flow past and through a porous square cylinder," Int. J. Heat Fluid Flow **31**, 141–153 (2010).

[7]P. Yu, Y. Zeng, T. S. Lee, X. B. Chen, and H. T. Low, "Steady flow around and through a permeable circular cylinder," Comput. Fluids **42**, 1–12 (2011).

[8]P. Yu, Y. Zeng, T. S. Lee, X. B. Chen, and H. T. Low, "Numerical simulation on steady flow around and through a porous sphere," Int. J. Heat Fluid Flow **36**, 142–152 (2012).

[9]C. Ellington, "Wing mechanics and take-off preparation of thrips (Thysanoptera)," J. Exp. Biol. **85**, 129–136 (1980).

[10]E. Barta and D. Weihs, "Creeping flow around a finite row of slender bodies in close proximity," J. Fluid Mech. **551**, 1–17 (2006).

[11]S. Taddei, C. Manes, and B. Ganapathisubramani, "Characterisation of drag and wake properties of canopy patches immersed in turbulent boundary layers," J. Fluid Mech. **798**, 27–49 (2016).

[12]G. Neale, N. Epstein, and W. Nader, "Creeping flow relative to permeable spheres," Chem. Eng. Sci. **28**, 1865–1874 (1973).

[13]M. Liu, C. Xie, M. Yao, and J. Yang, "Study on the near wake of a honeycomb disk," Exp. Therm. Fluid Sci. **81**, 33–42 (2017).

[14]W. W. Willmarth, N. E. Hawk, and R. L. Harvey, "Steady and unsteady motions and wakes of freely falling disks," Phys. Fluids **7**, 197 (1964).

[15]F. W. Roos and W. W. Willmarth, "Some experimental results on sphere and disk drag," AIAA J. **9**, 285–291 (1971).

[16]S. B. Field, M. Klaus, M. Moore, and F. Nori, "Chaotic dynamics of falling disks," Nature **388**, 252–254 (1997).

[17]P. C. Fernandes, F. Risso, P. Ern, and J. Magnaudet, "Oscillatory motion and wake instability of freely rising axisymmetric bodies," J. Fluid Mech. **573**, 479–502 (2007).

[18]A. Shenoy and C. Kleinstreuer, "Flow over a thin circular disk at low to moderate Reynolds numbers," J. Fluid Mech. **605**, 253–262 (2008).

[19]D. Fabre, F. Auguste, and J. Magnaudet, "Bifurcations and symmetry breaking in the wake of axisymmetric bodies," Phys. Fluids **20**, 051702 (2008).

[20]F. Auguste, D. Fabre, and J. Magnaudet, "Bifurcations in the wake of a thick circular disk," Theor. Comput. Fluid Dyn. **24**, 305–313 (2010).

[21]Z.-G. Feng and E. E. Michaelides, "Motion of a permeable sphere at finite but small Reynolds numbers," Phys. Fluids **10**, 1375–1383 (1998).

[22]I. Castro, "Wake characteristics of two-dimensional perforated plates normal to an air-stream," J. Fluid Mech. **46**, 599–609 (1971).

[23]T.-C. Jue, "Numerical analysis of vortex shedding behind a porous square cylinder," Int. J. Numer. Methods Heat Fluid Flow **14**, 649–663 (2004).

[24]X. Chen, P. Yu, S. Winoto, and H.-T. Low, "Numerical analysis for the flow past a porous square cylinder based on the stress-jump interfacial-conditions," Int. J. Numer. Methods Heat Fluid Flow **18**, 635–655 (2008).

[25]A. Cheer and M. Koehl, "Paddles and rakes: Fluid flow through bristled appendages of small organisms," J. Theor. Biol. **129**, 17–39 (1987).

[26]M. Koehl, "The morphology and performance of suspension-feeding appendages," J. Theor. Biol. **105**, 1–11 (1983).

[27]S. Sunada, H. Takashima, T. Hattori, K. Yasuda, and K. Kawachi, "Fluid-dynamic characteristics of a bristled wing," J. Exp. Biol. **205**, 2737–2744 (2002).

[28]P. C. Carman, "Fluid flow through granular beds," Trans. Inst. Chem. Eng. **15**, 150–166 (1937).

[29]J. Kozeny, *Über kapillare Leitung des Wassers im Boden: (Aufstieg, Versickerung und Anwendung auf die Bewässerung)* (Hölder-Pichler-Tempsky, 1927).

[30]D. R. Arcas and L. G. Redekopp, "Aspects of wake vortex control through base blowing/suction," Phys. Fluids **16**, 452–456 (2004).

[31]I. Viola, P. Bot, and M. Riotte, "On the uncertainty of CFD in sail aerodynamics," Int. J. Numer. Methods Fluids **72**, 1146–1164 (2013).

[32]P. J. Roache, "Verification of codes and calculations," AIAA J. **36**, 696–702 (1998).